

# A Variable Curvature Model for Multi-Backbone Continuum Robots to Account for Inter-Segment Coupling and External Disturbance

Yuyang Chen , Baibo Wu, Jiabin Jin, and Kai Xu , *Member, IEEE*

**Abstract**—Multi-backbone continuum robots demonstrated potentials for dexterous manipulation with proper payload capability in minimally invasive surgeries. Most prior works assume constant curvature shapes of the continuum segments in the modeling and control of the multi-backbone continuum robots. The actuation coupling effects between adjacent continuum segments and the segments' variable curvature shapes under environmental interactions have not been fully addressed by a static-kinematic model specifically for multi-backbone continuum robots. This letter hence proposes a variable curvature model for multi-backbone continuum robots with relatively low bending curvature based on the Cosserat rod theory. The model focuses on the major factors that affect the robot's shape: the length-prescribed push-pull actuation, the elastic elongation of the backbone rods, and the external loads. With five assumptions made to simplify the constraints in the multi-backbone continuum robot, a compact statics-kinematics formulation is derived with computational performance acceptable for real-time control. Experiments were conducted on a continuum robotic system to quantify the modeling accuracy and computational efficiency. The proposed model was shown to have substantially improved accuracy over the constant curvature model. The average computational time for solving the inverse kinematics was 0.7ms on a 2.6 GHz Intel i7-5600U platform, which is promising for real-time control.

**Index Terms**—Surgical robotics: Laparoscopy, compliant joints and mechanisms, continuum robots, kinematics.

## I. INTRODUCTION

CONTINUUM robots are envisioned as a promising candidate for MIS (Minimally Invasive Surgery), due to their appealing merits of inherent compliance, scalability, design compactness and dexterity in confined spaces [1]. In the last

Manuscript received October 15, 2020; accepted February 3, 2021. Date of publication February 11, 2021; date of current version March 2, 2021. This letter was recommended for publication by Associate Editor C. Rucker and Editor P. Valdastri upon evaluation of the reviewers' comments. This work was supported in part by the National Natural Science Foundation of China under Grant 51722507, in part by the National Key R&D Program of China under Grant 2017YFC0110800, and in part by the Interdisciplinary Program of Shanghai Jiao Tong University under Grant YG2019QNB26. (*Corresponding author: Kai Xu.*)

Yuyang Chen is with the RII Lab (Laboratory of Robotics Innovation and Intervention), UM-SJTU Joint Institute, Shanghai Jiao Tong University, Shanghai 200240, China (e-mail: supandoria@sjtu.edu.cn).

Baibo Wu and Kai Xu are with the School of Mechanical Engineering, Shanghai Jiao Tong University, Shanghai 200240, China (e-mail: wubaibo@sjtu.edu.cn; k.xu@sjtu.edu.cn).

Jiabin Jin is with the Department of General Surgery, Ruijin Hospital, School of Medicine, Shanghai Jiao Tong University, Shanghai 200025, China (e-mail: jjb11501@rjh.com.cn).

Digital Object Identifier 10.1109/LRA.2021.3058925

two decades, numerous surgical platforms based on continuum robots have been developed, for example in cardiovascular surgery [2], neurosurgery [3], endoscopic surgery [4], laparoscopic surgery [5], etc.

Extending continuum robot applications in MIS is majorly challenged by their drawbacks of low precision and payload capability, compared to their rigid-linked counterparts.

Although the precision can be improved via motion calibration and actuation compensation [6], [7] while using the widely adopted constant curvature kinematics model [8], the accuracy of the constant curvature model is deteriorated with the occurred effects of tendon elongation/slackness [9], coupled bending [10], and external disturbances. A versatile variable curvature model is hence desirable to better harness continuum robots when a robot's shape is co-determined by actuation and environmental interactions.

The demand to improve structural rigidity of continuum surgical manipulators stimulates the designs of multi-backbone continuum mechanism [11] and subsequently the dual continuum mechanism [5]. Such designs have been applied in laparoscopic surgery [12], transurethral surgery [13], throat surgery [14], endoscopic surgery [15], etc. Continuum robots in these procedures are required to apply forces (e.g., dissection and knot-tying) at the distal ends. The constant curvature kinematics model that was adopted in most multi-backbone continuum robots [16], [17] cannot accurately describe the shapes under external loads. It is hence worthy exploring a variable curvature model for multi-backbone continuum robots to account for external disturbances.

This letter hence aims at presenting a static kinematic model for multi-backbone continuum robots using a variable curvature formulation. The model is expected to benefit the control precision of continuum surgical robots while preserving safe interaction due to a continuum robot's structural compliance, during minimally invasive procedures.

## A. Related Work and Contributions

To characterize the deformation of continuum robots under external loads, various static kinematic models have been developed, using approximation-based methods or an exact deformation-oriented approach.

The approximation-based methods include the piecewise constant curvature model [18]–[21], the Bézier curve fitting [22], the pseudo rigid body model [23], etc. These models make approximations that reduce the dimensionality of the shape using a finite number of variables.

TABLE I  
NOMENCLATURES IN THE VARIABLE CURVATURE MODEL

Symbol	Definition
$i$	Index of the continuum segment, $i = 1, 2, \dots, n$ . The segments are indexed in an ascending order from the base segment to the most distal segment.
$j$	Index of the backbones that are attached to the end ring of each continuum segment, $j = 1, 2, \dots, m$ . Indexing of the backbone ascends with the rotation angle from $\mathbf{x}_0$ to $\mathbf{r}_{ij}$ about $\mathbf{z}_0$ , referring to Fig. 1(b). The segment index always precedes the backbone index.
$\mathbf{r}_{ij}$	Vectors indicating the coordinates of the $j^{\text{th}}$ backbone in the $i^{\text{th}}$ continuum segment in frame $\{0\}$ .
$s_0, s_{ij}$	Arc length parameters for the central axis and for the $j^{\text{th}}$ rod in the $i^{\text{th}}$ continuum segment. Variables without specifying the arc length parameter vary with respect to $s_0$ .
$\lambda_i$	Arc length of the central axis from the $i^{\text{th}}$ end ring to the 1 <sup>st</sup> base ring.
$L_0(s_0), L_{ij}(s_0)$	The lengths of the central axis and the $j^{\text{th}}$ rod in the $i^{\text{th}}$ continuum segment from the cross section at $s_0 = 0$ to the cross section at $s_0$ .
$L_{\text{all},i}$	The total length of each rod the $i^{\text{th}}$ continuum segment, routed from the actuation mechanism to the $i^{\text{th}}$ end ring.
$\mathbf{q}_{ai}$	$\mathbf{q}_{ai} = [q_{ai1} \dots q_{aim}]^T$ is the actuation length vector for the $i^{\text{th}}$ continuum segment.
$q_{ij}(s_0)$	$q_{ij}(s_0) = L_{ij}(s_0) - L_0(s_0)$ is the length difference between the $j^{\text{th}}$ rod in the $i^{\text{th}}$ continuum segment and the central axis. $\mathbf{q}_i = [q_{i1} \dots q_{im}]^T$ .
$\mathbf{p}_0(s_0), \mathbf{R}_0(s_0)$	The position vector and rotation matrix of the segment body frame $\{0\}$ as a function of $s_0$ .
$\mathbf{p}_{ij}(s_0), \mathbf{R}_{ij}(s_0)$	The position vector and rotation matrix of the backbone rod body frame $\{ij\}$ as a function of $s_0$ .
$\varepsilon_{ij}$	Elongation strain in the $j^{\text{th}}$ rod of the $i^{\text{th}}$ continuum segment.
$\omega_0(s_0), \mathbf{u}_0(s_0)$	Linear and angular rate change of $\{0\}$ with respect to $s_0$ .
$\mathbf{v}_{ij}(s_0), \mathbf{u}_{ij}(s_0)$	Linear and angular rate change of $\{ij\}$ with respect to $s_0$ .
$\mathbf{n}_0(s_0), \mathbf{m}_0(s_0)$	Internal force and moment transmitted by the structural constraint at $s_0$ .
$\mathbf{n}_{ij}(s_0), \mathbf{m}_{ij}(s_0)$	Internal force and moment in the $j^{\text{th}}$ rod in the $i^{\text{th}}$ continuum segment at $s_0$ .
$\mathbf{n}(s_0), \mathbf{m}(s_0)$	Total internal force and moment in the continuum segment at $s_0$ .
$\mathbf{f}_e(s_0), \mathbf{l}_e(s_0)$	Distributed external body force and moment acting on the continuum segment.
$\mathbf{n}_{ei}, \mathbf{m}_{ei}$	External force and moment acting on the end of the $i^{\text{th}}$ continuum segment.

On the other hand, the variable curvature model, by assuming a continuous shape, can achieve improved modeling accuracy at the expense of a higher computational cost. Elastic rod theories or energy methods (e.g., in [24]) are often employed to provide mechanical governing equations. The Cosserat rod theory has been used to model the central backbone of tendon-driven continuum robots [25] and pre-curved concentric tubes [26], as well as the legs in the parallel continuum robots without or with intermediate constraints disks, as in [27] and [28], respectively.

The parallel continuum robot with intermediate constraints disks studied in [28] has six actuators for pushing or pulling each leg. Since the interactions between the legs and the intermediate constraints disks as well as the distal platform shall all be examined, the derived Cosserat rod model is less computationally efficient and real-time inverse kinematics solutions were only pursued for the cases with no intermediate constraints disks, instead of with the constraints disks [28].

The intermediate constraints disks that are incorporated into multi-backbone continuum robots can in fact enhance the structural stability. In order to enjoy the enhanced structural integrity and the improved modeling accuracy brought by the Cosserat

rod theory with a hope for real-time implementation of the inverse kinematics, this letter hence proposes a variable curvature model that utilizes structure-induced assumptions to generate a compact and computationally efficient formulation. Numerical analyses and experimental results validated the variable curvature model with the inverse kinematics implemented in a real-time control loop, exhibiting improved modeling accuracy of a 2-segment continuum robot under inter-segment coupling and external disturbance, compared to the constant curvature model.

## B. Organization

Organization of this letter is as follows. In Section II, the variable curvature model derivation is presented in detail. In Section III, the experimental validation on the modeling accuracy and computing efficiency are elaborated. A brief discussion on the model is presented in Section IV. Conclusion and future work are summarized in Section V.

## II. MODEL FORMULATION

In this section, the classical Cosserat rod model is first summarized. For continuum segments consisting of multiple Cosserat backbone rods and constrained by multiple spacer rings, five assumptions are made to simplify the formulation. The model of the continuum segment is then developed. The nomenclatures used in the model are listed in Table I.

### A. The Classical Cosserat Rod Model

Let  $\{w\} = \{\mathbf{x}_w, \mathbf{y}_w, \mathbf{z}_w\}$  be a fixed known *reference frame*. Let the shape of the  $j^{\text{th}}$  backbone rod in the  $i^{\text{th}}$  continuum segment be represented by a spatial curve parameterized by arc length  $s_{ij}$ . The deformation of the rod is described by the *backbone rod body frame*  $\{ij\} = \{\mathbf{x}_{ij}(s_{ij}), \mathbf{y}_{ij}(s_{ij}), \mathbf{z}_{ij}(s_{ij})\}$  moving along the curve, where axes  $\mathbf{x}_{ij}(s_{ij})$  and  $\mathbf{y}_{ij}(s_{ij})$  define the rod's cross section plane. The rate change of frame  $\{ij\}$  with respect to  $s_{ij}$  indicate the strain vectors  $\mathbf{u}_{ij}(s_{ij})$  and  $\mathbf{v}_{ij}(s_{ij})$ , as given by the equations:

$$\dot{\mathbf{p}}_{ij}(s_{ij}) = \mathbf{R}_{ij}(s_{ij})\mathbf{v}_{ij}(s_{ij}), \quad \dot{\mathbf{R}}_{ij}(s_{ij}) = \mathbf{R}_{ij}(s_{ij})\hat{\mathbf{u}}_{ij}(s_{ij}), \quad (1)$$

where the operator  $(\hat{\cdot})$  maps  $\mathfrak{R}^3$  to  $\mathfrak{so}(3)$ .

The mechanics model of the rod describing the evolution of internal force and moment in the rod  $\mathbf{n}_{ij}(s_{ij})$  and  $\mathbf{m}_{ij}(s_{ij})$  is given by the differential equations:

$$\begin{aligned} \dot{\mathbf{n}}_{ij}(s_{ij}) + \mathbf{f}_{eij}(s_{ij}) &= \mathbf{0}, \\ \dot{\mathbf{m}}_{ij}(s_{ij}) + \dot{\mathbf{p}}_{ij}(s_{ij}) \times \mathbf{n}_{ij}(s_{ij}) + \mathbf{l}_{eij}(s_{ij}) &= \mathbf{0}, \end{aligned} \quad (2)$$

where  $\mathbf{f}_{eij}(s_{ij})$  and  $\mathbf{l}_{eij}(s_{ij})$  are the distributed body force and moment acting on the rod.

The constitutive law relating the internal wrench and the deformation is assumed linear functions, as described by:

$$\begin{aligned} \mathbf{m}_{ij}(s_{ij}) &= \mathbf{R}_{ij}(s_{ij})\mathbf{K}_B(\mathbf{u}_{ij}(s_{ij}) - \mathbf{u}_{\min}), \\ \mathbf{n}_{ij}(s_{ij}) &= \mathbf{R}_{ij}(s_{ij})\mathbf{K}_E(\mathbf{v}_{ij}(s_{ij}) - \mathbf{v}_{\min}), \end{aligned} \quad (3)$$

where the matrices  $\mathbf{K}_B = \text{diag}(EI, EI, 2GI)$  and  $\mathbf{K}_E = \text{diag}(GA, GA, EA)$  are stiffness matrices determined by the Young's modulus  $E$ , shear modulus  $G$ , cross section area  $A$ , and second moment of inertia of the cross section  $I$  (assuming

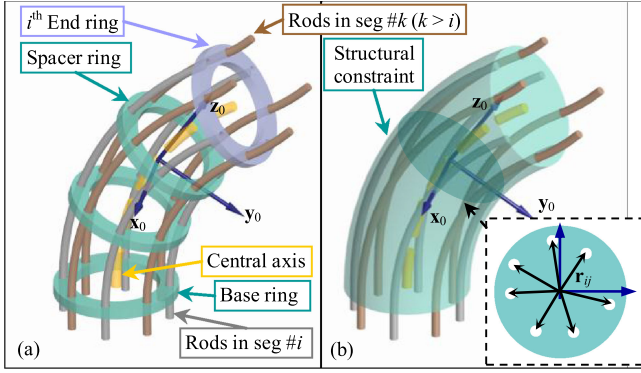


Fig. 1. Backbone rods in the continuum segments in (a) is assumed to be continuously constrained by the segment's cross section, as shown in (b).

isotropic material);  $\mathbf{v}_{\min} = [001]^T$  and  $\mathbf{u}_{\min} = \mathbf{0}$  represent the assumed unstressed state of the backbone rod.

### B. Model Assumptions

As shown in Fig. 1(a), the continuum segment under investigation consists of many rigid spacer rings, an end ring, a base ring, and several nitinol backbone rods that are attached to the end ring and slide freely in the holes of the spacer rings and the base ring. Because there are multiple stacked segments, the rods attached to the  $k^{\text{th}}$  end ring ( $k > i$ ) are also routed through the  $i^{\text{th}}$  segment via the holes in the spacer rings.

1) *Assumption 1. Torsion-Free, Inextensible Segment Bending:* Similar to (1), the *segment body frame*  $\{0\} = \{\mathbf{x}_0(s_0), \mathbf{y}_0(s_0), \mathbf{z}_0(s_0)\}$  is used to describe the central axis with the linear and angular velocities  $\mathbf{v}_0$  and  $\mathbf{u}_0$ :

$$\dot{\mathbf{p}}_0 = \mathbf{R}_0 \mathbf{v}_0, \dot{\mathbf{R}}_0 = \mathbf{R}_0 \hat{\mathbf{u}}_0. \quad (4)$$

The shape of the segment (i.e., its central axis) is considered rigid in torsion and extension. This can be physically achieved via using outer sheath tubes. The linear and angular velocities hence follow:

$$\mathbf{v}_0|_z = 1, \mathbf{u}_0|_z = 0. \quad (5)$$

2) *Assumption 2. Continuous Constraint:* As illustrated in Fig 1(b), the backbone rods are first treated as being continuously constrained by the segment structure, based on the small spacing between the rings. This reduces model complexity by avoiding solving the individual shapes of the rods. The segment's shape is hence represented by its imaginary central axis.

The rods can be parameterized using the central axis arc length  $s_0$ . The locations of the rods in every cross section defined by axes  $\mathbf{x}_0$  and  $\mathbf{y}_0$  are specified by the vectors  $\mathbf{r}_{ij}$ :

$$\mathbf{R}_0(\mathbf{p}_{ij} - \mathbf{p}_0) - \mathbf{r}_{ij} = \mathbf{0}. \quad (6)$$

This assumption also leads to the fact that frame  $\{ij\}$  and frame  $\{0\}$  are identical in orientation if no initial-twisting is added in the rod:

$$\mathbf{R}_{ij} = \mathbf{R}_0. \quad (7)$$

The local radii of curvature for the rods and the central axis are therefore related by:

$$\mathbf{u}_{ij} = \mathbf{u}_0 / (1 + \mathbf{e}_3^T (\hat{\mathbf{u}}_0 \mathbf{r}_{ij})). \quad (8)$$

where  $\mathbf{e}_3 = [001]^T$ .

3) *Assumption 3. Small Bending Curvature:* One important assumption to facilitate the model computation is the approximation as in (9). This assumption usually holds for continuum surgical manipulators whose bending curvature is relatively small. For example, applying this assumption on the continuum robot described in Section III.A leads to an approximation error of 0.364%. However, readers should check the approximation error based on their own robot designs before applying this assumption.

$$\sum_{j=1}^m \mathbf{u}_{ij} = \sum_{j=1}^m \mathbf{u}_0 / (1 + \mathbf{e}_3^T (\hat{\mathbf{u}}_0 \mathbf{r}_{ij})) \approx m \mathbf{u}_0. \quad (9)$$

4) *Assumption 4. Frictionless Contact:* Frictionless contact is often assumed for the multi-backbone continuum mechanisms with push-pull actuation, as in [28], [29].

By assuming frictionless contact between the rods and the constraint structure, (6) implies an identical shear and constant elongation strains in the rods:

$$\mathbf{v}_{ij} = \mathbf{v}_0 + [0 \ 0 \ \varepsilon_{ij}]^T. \quad (10)$$

5) *Assumption 5. Differential Actuation and Elongation:* All the backbone rods are actuated in a push-pull mode in a coordinated manner, bending the segment towards a certain direction. This bending can always be realized by a pair of rods. This means the actuation lengths  $\mathbf{q}_{ai}$  is equivalent to two effective actuation length  $\pm \bar{q}_{ai}$  in the locations  $\pm \bar{\mathbf{r}}_i$ . This can be formulated as a constraint:

$$q_{aij} / \|\mathbf{r}_{ij}\| = \bar{q}_{ai} \cos(\delta_{ij} - \bar{\delta}_i) / \|\bar{\mathbf{r}}_i\|, \quad (11)$$

where  $\delta_{ij}$  and  $\bar{\delta}_i$  are the rotation angles from  $\mathbf{x}_0$  to  $\mathbf{r}_{ij}$  or  $\bar{\mathbf{r}}_i$  about  $\mathbf{z}_0$ . Defining the vector  $\boldsymbol{\mu}_{ai}$  as:

$$\boldsymbol{\mu}_{ai} := (\bar{q}_{ai} / \|\bar{\mathbf{r}}_i\|) \mathbf{e}_3 \times \bar{\mathbf{r}}_i. \quad (12)$$

(11) can then be put in a matrix form:

$$\mathbf{q}_{ai} = [\hat{\mathbf{r}}_{i1} \mathbf{e}_3 \cdots \hat{\mathbf{r}}_{im} \mathbf{e}_3]^T \boldsymbol{\mu}_{ai} := \mathbf{Q}_i^T \boldsymbol{\mu}_{ai}. \quad (13)$$

Next, the elongation strains in the rods are also assumed to be differential:

$$[\varepsilon_{i1} \cdots \varepsilon_{im}]^T = \mathbf{Q}_i^T \boldsymbol{\mu}_{\varepsilon i}, \quad (14)$$

where  $\boldsymbol{\mu}_{\varepsilon i}$  is an arbitrary vector in  $\mathfrak{R}^3$ .

### C. Model Derivation

Based on the aforementioned assumptions, it is now straightforward to derive the variable curvature model for the continuum segment.

Firstly, the mechanics model is obtained from the equilibrium of forces and moments in an infinitesimal element, as illustrated in Fig. 2. The force balance equation in a differential form is as follows.

$$\dot{\mathbf{n}}_0 + \sum_{k=i}^n \sum_{j=1}^m \dot{\mathbf{n}}_{kj} + \mathbf{f}_e = \mathbf{0} \quad (15)$$

The total internal force is defined as follows.

$$\mathbf{n} := \mathbf{n}_0 + \sum_{k=i}^n \sum_{j=1}^m \mathbf{n}_{kj} \quad (16)$$

(15) then becomes (17).

$$\dot{\mathbf{n}} + \mathbf{f}_e = \mathbf{0}. \quad (17)$$

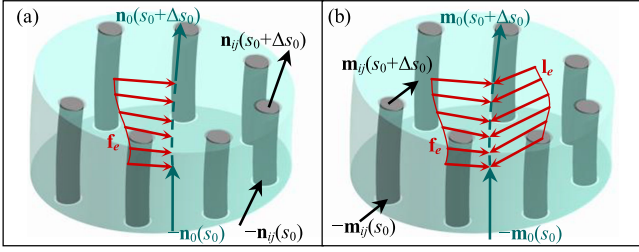


Fig. 2. The balance of (a) forces and (b) moments in a slice of continuum segment.

The moment balance equation is in (18).

$$\begin{aligned} \dot{\mathbf{m}}_0 + \sum_{k=i}^n \sum_{j=1}^m \dot{\mathbf{m}}_{kj} + \dot{\mathbf{p}}_0 \times \mathbf{n}_0 + \mathbf{p}_0 \times \dot{\mathbf{n}}_0 \\ + \sum_{k=i}^n \sum_{j=1}^m (\dot{\mathbf{p}}_{kj} \times \mathbf{n}_{kj} + \mathbf{p}_{kj} \times \dot{\mathbf{n}}_{kj}) + \mathbf{p}_0 \times \mathbf{f}_e + \mathbf{l}_e = \mathbf{0} \end{aligned} \quad (18)$$

Similarly, the total moment can be defined as in (19).

$$\mathbf{m} := \mathbf{m}_0 + \sum_{k=i}^n \sum_{j=1}^m \mathbf{m}_{kj} \quad (19)$$

(19) then yields (20).

$$\begin{aligned} \mathbf{0} = \dot{\mathbf{m}} + \dot{\mathbf{p}}_0 \times \mathbf{n} + \mathbf{l}_e \\ + \mathbf{R}_0 \sum_{k=i}^n \sum_{j=1}^m [\mathbf{r}_{kj} \times (\hat{\mathbf{u}}_0 \mathbf{K}_E \tilde{\mathbf{v}}_{kj}) + (\hat{\mathbf{u}}_0 \mathbf{r}_{kj}) \times (\mathbf{K}_E \tilde{\mathbf{v}}_{kj})], \end{aligned} \quad (20)$$

where  $\tilde{\mathbf{v}}_{kj} = \mathbf{v}_{kj} - \mathbf{v}_{\min} = \mathbf{v}_0 - (1 - \varepsilon_{kj})\mathbf{e}_3$ .

Secondly, it shall be noted that the projections of  $\mathbf{n}$  in (16) and  $\mathbf{m}$  in (19) in the cross section (i.e., the shearing force and the bending moment) are transmitted by the rods. Utilizing (3), (9) and (14), a constitutive law for  $\mathbf{n}$  and  $\mathbf{m}$  is as follows.

$$(n - i + 1)m\mathbf{v}_0|_{xy} = [\mathbf{K}_E^{-1} \mathbf{R}_0^T \mathbf{n}]|_{xy}, \quad (21)$$

$$(n - i + 1)m\mathbf{u}_0|_{xy} = [\mathbf{K}_B^{-1} \mathbf{R}_0^T \mathbf{m}]|_{xy}. \quad (22)$$

Lastly, the backbone rod lengths are related to the central axis. The length of the  $j^{\text{th}}$  rod in the  $i^{\text{th}}$  segment, from the cross section at  $s_0 = 0$  to the cross section at  $s_0$ , is calculated by (23).

$$L_{ij}(s_0) = \int_0^{s_0} \|\dot{\mathbf{p}}_{ij}(\xi)\| d\xi = \int_0^{s_0} \|\mathbf{v}_0(\xi)\| + \mathbf{e}_3^T \hat{\mathbf{r}}_{ij} \mathbf{u}_0(\xi) d\xi \quad (23)$$

where  $\int_0^{s_0} \|\mathbf{v}_0(\xi)\| d\xi = L_0(s_0)$  in the right-hand side is the corresponding length of the central axis.

Defining the *rod length increment*  $\mathbf{q}_i(s_0) = [q_{i1}(s_0) \dots q_{im}(s_0)]^T$  as  $q_{ij}(s_0) := L_{ij}(s_0) - L_0(s_0)$ , and a set of differential equations can be formulated as in (24).

$$\dot{\mathbf{q}}_i(s_0) = \mathbf{Q}_i^T \mathbf{u}_0(s_0). \quad (24)$$

#### D. Boundary Conditions

The abovementioned equations (4–5), (17), (20–22), and (24) form a set of differential equations. They are summarized

as in (25), to be solved with proper boundary conditions. For the forward kinematics problems, the lengths of the rods are specified by the differential actuation  $\mathbf{q}_{ai}$  and subject to elastic elongations. The boundary conditions on rod length increments at the end of each segment  $s_0 = \lambda_i$  is given by (26).

$$\dot{\mathbf{p}}_0 = \mathbf{R}_0 \mathbf{v}_0, \quad \dot{\mathbf{R}}_0 = \mathbf{R}_0 \hat{\mathbf{u}}_0,$$

$$(n - i + 1)m\mathbf{v}_0|_{xy} = [\mathbf{K}_E^{-1} \mathbf{R}_0^T \mathbf{n}]|_{xy}, \quad \mathbf{v}_0|_z = 1,$$

$$(n - i + 1)m\mathbf{u}_0|_{xy} = [\mathbf{K}_B^{-1} \mathbf{R}_0^T \mathbf{m}]|_{xy}, \quad \mathbf{u}_0|_z = 0,$$

$$\mathbf{0} = \dot{\mathbf{n}} + \mathbf{f}_e,$$

$$\mathbf{0} = \dot{\mathbf{m}} + \dot{\mathbf{p}}_0 \times \mathbf{n} + \mathbf{l}_e$$

$$+ \mathbf{R}_0 \sum_{k=i}^n \sum_{j=1}^m [\mathbf{r}_{kj} \times (\hat{\mathbf{u}}_0 \mathbf{K}_E \tilde{\mathbf{v}}_{kj}) + (\hat{\mathbf{u}}_0 \mathbf{r}_{kj}) \times (\mathbf{K}_E \tilde{\mathbf{v}}_{kj})],$$

$$\dot{\mathbf{q}}_i = \mathbf{Q}_i^T \mathbf{u}_0. \quad (25)$$

$$\mathbf{q}_i(\lambda_i) = \mathbf{q}_{ai} + L_{\text{all},i}[\varepsilon_{i1} \dots \varepsilon_{im}]^T = \mathbf{q}_{ai} + L_{\text{all},i} \mathbf{Q}_i^T \boldsymbol{\mu}_{\varepsilon i}. \quad (26)$$

The force and moment balance equations at  $s_0 = \lambda_i$  can be obtained similarly to the formulations in (15) and (18):

$$-\mathbf{n}^+(\lambda_i) + \mathbf{n}^-(\lambda_i) + \mathbf{n}_{ei} = \mathbf{0}, \quad (27)$$

$$-\mathbf{m}^+(\lambda_i) + \mathbf{m}^-(\lambda_i) + \mathbf{m}_{ei} - \mathbf{R}_0 \sum_{j=1}^m \mathbf{r}_{ij} \times (\mathbf{K}_E \tilde{\mathbf{v}}_{ij}) = \mathbf{0}, \quad (28)$$

where the superscripts  $(-)$  or  $(+)$  represent the limits of quantities obtained by decreasing or increasing  $s_0$ . For the most distal segment ( $i = n$ ), the terms  $\mathbf{n}^-(\lambda_n)$  and  $\mathbf{m}^-(\lambda_n)$  vanish.

For inverse kinematics problems, the tip pose is specified by  $\mathbf{p}_g$  and  $\mathbf{R}_g$ , whereas the actuation lengths are unknown. The boundary condition (26) is replaced by the following ones:

$$\mathbf{p}_0(\lambda_n) - \mathbf{p}_g = \mathbf{0}, \quad (29)$$

$$(\log(\mathbf{R}_0^T(\lambda_n) \mathbf{R}_g))^\vee = \mathbf{0}. \quad (30)$$

#### E. Numerical Solution

The forward and the inverse kinematics problems are represented by the abovementioned boundary value problems (BVPs) that are numerically solved using a shooting method. Boundary condition residuals are calculated via numerical integrations on the corresponding initial value problems (IVPs) with guessed unknown kinematics variables. The boundary residuals are obtained via numerical integration using the step-forward finite difference method (a.k.a., the forward Euler method) with respect to the centerline length  $s_0$  from the base to the distal tip. The kinematics variables are then iteratively updated by eliminating the boundary condition residuals in a gradient-based optimization framework. The gradients are calculated using the finite difference method. For an  $n$ -segment continuum robot with an arbitrary number of rods in each segment, the forward kinematics problem contains  $6 + 2n$  unknowns ( $\mathbf{n}(0)$ ,  $\mathbf{m}(0)$ , and two components in  $\boldsymbol{\mu}_{\varepsilon i}$ ) and a  $(6 + 2n)$ -DoF boundary condition (for  $\mathbf{n}$ ,  $\mathbf{m}$ , and  $\mathbf{q}_i$ ), whereas the inverse kinematics problem contains the same  $6 + 2n$  unknowns and a 12-DoF boundary condition (for  $\mathbf{n}$ ,  $\mathbf{m}$ ,  $\mathbf{p}_0$ , and  $\mathbf{R}_0$ ). The reduced dimensions of the problems

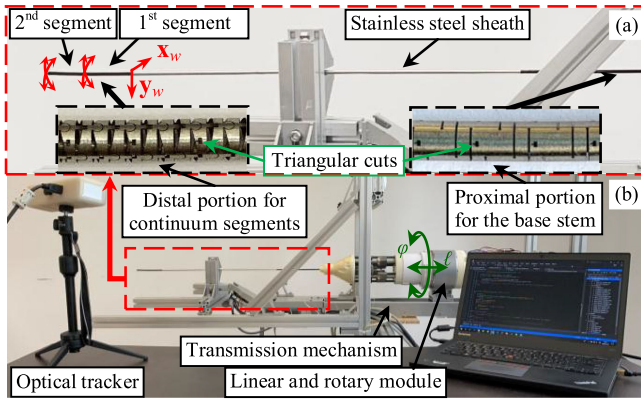


Fig. 3. The continuum robotic system for experimental evaluation: (a) the continuum robot tool and (b) the experimental setup.

entail modest computational cost, and can be effectively solved in real time applications.

In the following experiments, the abovementioned numerical resolution was implemented with C++ on a laptop with 2.60 GHz Intel Core i7-5600U CPU and 12 G RAM. Iterations were terminated if the norm of the residual errors for the boundary conditions were less than  $10^{-4}$  (the units were meter and radian).

### III. EXPERIMENTAL EVALUATION

In this section, the proposed variable curvature model is validated on a continuum robotic system.

#### A. System Description and Experiment Setup

As shown in Fig. 3(a), a continuum robotic system for minimally invasive procedures was adopted to experimentally validate the proposed variable curvature model. The robotic system, which is also used in a previous study [30], includes an exchangeable continuum robot tool and its actuation unit.

The continuum robot tool consists of two multi-backbone continuum segments, stacked on a long base stem. The base stem was flexible to help the continuum segments pass through curved access lumens such that the tool can be used in a transurethral application as in [31]. Each continuum segment includes four  $\phi 0.37$ -mm nitinol rods. These rods pass through the  $\phi 0.42$ -mm holes that are evenly distributed on a  $\phi 1.7$ -mm pitch circle in the spacer rings. The spacer rings with 1-mm thickness and an  $\phi 2.38$ -mm outer diameter are welded inside a stainless steel outer tube with an inner diameter of 2.4 mm and an outer diameter of 2.7 mm, via the triangular cuts that are cut on the outer tube by laser cutting. The spacer rings are welded every 5 mm. 113 spacer rings were used. A  $\phi 1$ -mm internal lumen is spared to pass the electric wire for an electrosurgical cautery hook end-effector.

The cut patterns on the stainless steel outer tube contain two portions. The distal portion is with passive revolute joints for the segment's tight bending, while the proximal portion is with helically arranged straight cuts.

Eight rods in the continuum segments (four for the 1<sup>st</sup> and the 2<sup>nd</sup> segments respectively) were routed to the transmission mechanism of the continuum robot tool, pushed and pulled by four sets of twin-screws (including twin-screw, nuts, guiding rail etc.). Push-pull actuation bends the continuum robot tool.

TABLE II  
STRUCTURAL PARAMETERS OF THE CONTINUUM ROBOT

Parameters	Values
Rod diameter	0.37 mm
Young's modulus for nitinol	50 GPa
Lengths of the 1 <sup>st</sup> segment, 2 <sup>nd</sup> segment, and the end-effector	43 mm, 25 mm, and 10 mm
Rod total lengths $L_{all,1}$ and $L_{all,2}$	543 mm and 568 mm
Rod distribution radius	$\ r_{ij}\  = 0.85$ mm
Stiffness of the notched outer tube	$\mathbf{K}_C = 42.7\mathbf{K}_B$

The transmission mechanism was mounted on a rotary module that is translated by a linear module for longitudinal feeding motion. The rotary module houses motors to drive the twin-screw, as well as rotates the continuum robot tool. Hence, the continuum robot tool can realize 6-DoF motions (1 feeding, 1 rotation, and 2 bending for each segment).

In the experiments, the continuum segments and the base stem were longitudinally constrained by a stainless steel sheath, which was fixed to the linear module.

The reference frame  $\{w\}$  was attached to end of the sheath with  $\mathbf{z}_w$  in the longitudinal feeding direction and  $\mathbf{y}_w$  in the gravity direction, as in Fig. 3(b). An optical tracker (Micron Tracker SX60, Claron Technology Inc.) with about 0.3-mm sensing accuracy was employed to obtain the actual robot shapes or tip positions with ancillary markers or pointers.

The portion of the stainless steel tube with passive joints is assumed to have negligible effects on the continuum segment's bending. When the flexible base stem was fed further enough to extend the notch-patterned portion out of the stainless steel sheath, this portion will be passively deflected by the bending of the 1<sup>st</sup> segment. This portion was hence modeled as a separate continuum segment with an additional central Cosserat rod with bending stiffness  $\mathbf{K}_C$ . Denoting the feeding length as  $\ell$ , the base stem is treated as an extension of the 1<sup>st</sup> continuum segment with the constitutive equation:

$$\mathbf{u}_0|_{xy} = \left[ \left( \frac{1}{2m} \mathbf{K}_B + \mathbf{K}_C \right)^{-1} \mathbf{R}_0^T \mathbf{m} \right] |_{xy} \quad (31)$$

for  $0 \leq s_0 \leq \ell$ , where  $m = 4$ , since each segment has 4 rods.

Specifically, the inverse kinematics problem for the continuum robot was solved by formulating the initial conditions at the distal end  $s_0 = \lambda_2$  and evaluating boundary conditions at  $s_0 = 0$ . As such, the initial conditions are

$$\begin{aligned} \mathbf{p}_0(\lambda_2) &= \mathbf{p}_g, \mathbf{R}_0(\lambda_2) = \mathbf{R}_g, \\ \mathbf{n}(\lambda_2) &= \mathbf{n}_{e2}, \mathbf{m}(\lambda_2) = \mathbf{m}_{e2} - \mathbf{R}_0 \sum_{j=1}^m \mathbf{r}_{ij} \times (\mathbf{K}_E \tilde{\mathbf{v}}_{ij}) \end{aligned} \quad (32)$$

with only  $\varepsilon_{ij}$  (or  $\mu_{\varepsilon i}$ ) unknown. The boundary conditions were:

$$\mathbf{p}_0(0) = \mathbf{0}, [\log(\mathbf{R}_0(0))]^V|_{xy} = \mathbf{0}, \quad (33)$$

The base rotation angle  $\varphi$  is obtained from  $[\log(\mathbf{R}_0(0))]^V|_z$ . The structural and mechanical parameters of the continuum robot are listed in Table II.

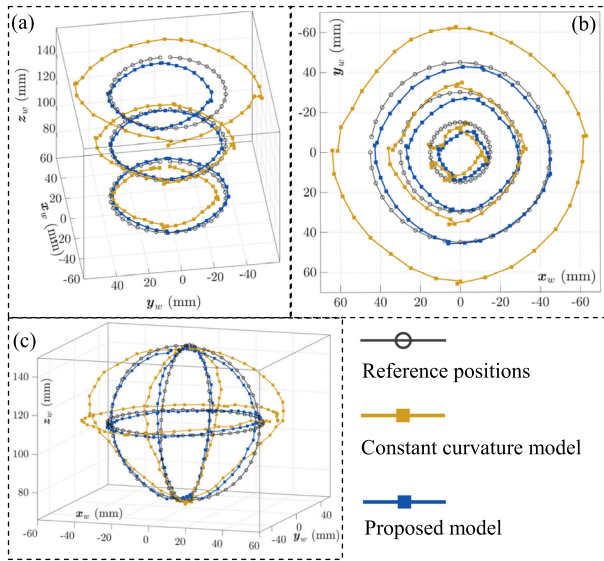


Fig. 4. Experiment results for tip positioning accuracy.

### B. Tip Positioning Accuracy

In the experiments quantifying tip positioning accuracy, the continuum robot was commanded to reach different target positions in its workspace, whereas the target orientations were all  $\mathbf{I}_{3 \times 3}$ . Three groups of targets were used to characterize the positioning performance. Both the variable curvature model and the constant curvature model with actuation compensation [6] were used and the results were compared.

In the first group, the targets were on three  $\phi 70$ -mm circles in parallel planes with base feeding  $\ell = 0, 40$ , and  $80$  mm. The measured and reference positions are presented in Fig. 4(a). The positioning errors of the constant curvature model went large as the length of the base stem increases, especially in the upper circle. In contrast, the proposed model exhibited improved accuracy, mainly owing to its capability to account the coupled deflections of the flexible base stem and the first segment. The average positioning errors for the proposed model for the targets in the bottom, middle and upper circles were  $3.37$  mm,  $5.27$  mm, and  $9.44$  mm, compared to  $6.58$  mm,  $6.65$  mm, and  $19.19$  mm for the constant curvature model, corresponding to the reductions of  $49.32\%$ ,  $20.73\%$ , and  $50.81\%$ , respectively.

In the second group, the targets were on three concentric circles in the plane with  $\ell = 40$  mm. The diameters of the circles were  $30, 60$ , and  $90$  mm. As shown in Fig. 4(b), the tip positions produced by the constant curvature model exhibited inconsistent accuracies in the radial direction, compared to the variable curvature model. This demonstrated the incapability of the bending calibration to capture the coupled bending between continuum segments adopted in the constant curvature model. The average positioning errors for the proposed model for the inner, middle, and outer circles were  $4.84$  mm,  $5.12$  mm, and  $6.36$  mm, compared to  $5.02$  mm,  $7.46$  mm, and  $19.72$  mm for the constant curvature model, corresponding to the reductions of  $3.59\%$ ,  $31.34\%$ , and  $68.83\%$ , respectively.

In the third group, the targets were on three mutually perpendicular circles with a diameter of  $80$  mm, as shown in Fig. 4(c). The average error for the proposed model was  $3.97$

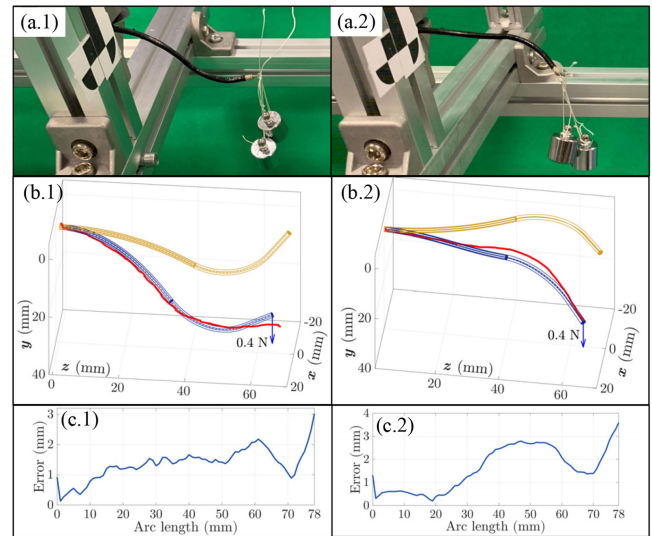


Fig. 5. The continuum robot shapes: (a) under two known external loading conditions; (b) the shapes obtained by the variable curvature model for the no-load condition (in yellow) and the tip-loaded conditions (in blue) with the actual shapes (in red) for the tip-loaded conditions; and (c) positioning errors along the arc length for loaded shapes.

mm, compared to  $9.33$  mm for the constant curvature model, corresponding to a  $57.45\%$  reduction.

### C. Shape Discrepancy With a Known Load

The proposed model was also evaluated on the robot with known external tip loads. As shown in Fig. 5(a), the robot was actuated to two configurations, one in the vertical plane and the other in the horizontal plane, and was loaded by a  $40$ -gram weight at its tip. In both configurations, the shapes were deflected from its unloaded states. By solving the forward kinematics of the variable curvature model, the loaded shapes were calculated and plotted in Fig. 5(b). The average error of the absolute deviation along the robot arc length for the proposed model in Fig. 5(b.1) and (b.2) were  $1.363$  mm and  $1.600$  mm respectively, whereas the corresponding maximum errors were  $3.022$  mm and  $3.595$  mm, as shown in Fig. 5(c.1) and (c.2). The loaded shapes were in acceptable conformity with the actual shape measured using the optical tracker.

### D. Real-Time Path Following

The proposed model was then tested in a real-time application. The continuum robot was commanded to follow a path in open-loop control, starting at  $[0090]^T$  mm and following a  $60$  mm  $\times$   $30$  mm rectangle, as indicated by the red line in Fig. 6.  $900$  target positions were uniformly distributed along the path with a  $0.2$ -mm spacing, whereas the target orientations were all  $\mathbf{I}_{3 \times 3}$ . Target positions were sequentially commanded to the robot every  $20$  ms. The solution for the last target position was used as the guesses for the next target.

Four experiments were conducted, respectively using the proposed variable curvature model and the constant curvature model, in conditions with no external load and with a  $20$ -gram weight loaded at the robot's tip.

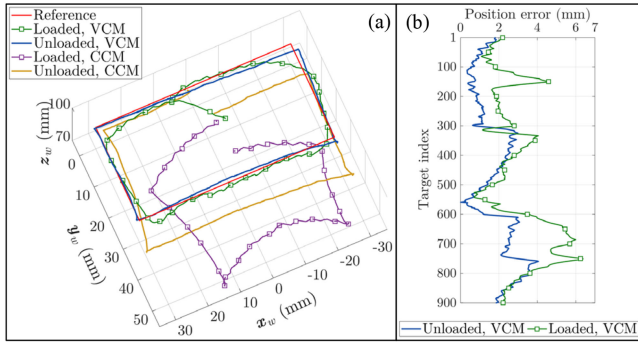


Fig. 6. (a) Path following experimental results with (b) the corresponding errors (VCM: variable curvature model, CCM: constant curvature model).

The actual tip positions were recorded by the tracker at 20 Hz and are also plotted in Fig. 6. The average computing time was 0.7001 ms. The maximum computing time was 5.109 ms, which was observed in solving for the first target in the loaded condition. The total duration of the path tracking was about 18.12 s. The variable curvature model exhibited better accuracy in both loaded and unloaded condition. Because the variable curvature model incorporated the external load information, it was able to correct the initially deflected tip position. For the variable curvature model, the mean, the standard deviation, and the maximal values of the tracking errors with respect to the target positions were 1.796 mm, 0.957 mm, and 4.053 mm, respectively, for the unloaded condition, and 2.865 mm, 1.367 mm, and 6.377 mm for the loaded condition. The performance of the variable curvature model deteriorated in the loaded condition, compared to its unloaded condition, which was owed to the effects of torsion, nonlinear elasticity, and drive backlashes, etc.

#### IV. DISCUSSION

The proposed model was demonstrated to have the ability to capture the shapes of continuum segments under inter-segment interactions and known external loads. And the external loads can be sensed, possibly adopting the force sensing techniques as in [29] and [32].

The constitutive equations in (21–22) are similar to the equations for a single Cosserat rod in (1–3) with a lumped stiffness. Nevertheless, it shall be noted that the multi-backbone continuum mechanism reacts to external wrenches in a different way compared to a single rod with lumped stiffness parameters. The essential difference lies in the additional variables  $\mathbf{q}_i(s_0)$  in the differential (25) and their corresponding boundary conditions in (26). This can be interpreted as constraints on the segment's deformation with actuation lengths partly offset by elastic elongations.

To illustrate the difference, a continuum segment composed of 4 backbone rods, each with a bending stiffness  $\mathbf{K}_B$  (the structural parameters are in Table II), was compared to a Cosserat rod with a bending stiffness of  $4\mathbf{K}_B$ . As in Fig. 7(a), the continuum segment was bent by the actuation lengths  $\mathbf{q}_a$ , whereas the Cosserat rod was actuated by a tip couple  $\mathbf{m}_a$  to reach the same orientation. For both cases, the tip deflection stiffness in response to tip external forces was examined.

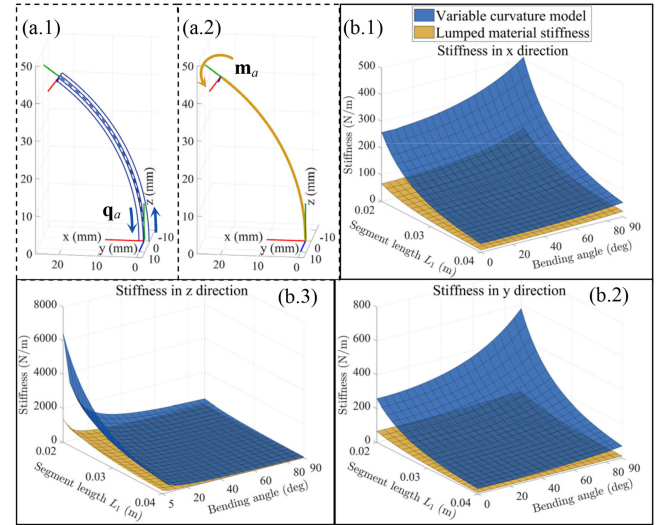


Fig. 7. Comparison between (a.1) the proposed variable curvature model and (a.2) the Cosserat rod model with lumped stiffness parameters: (b) deflection stiffness for different segment lengths and bending angles.

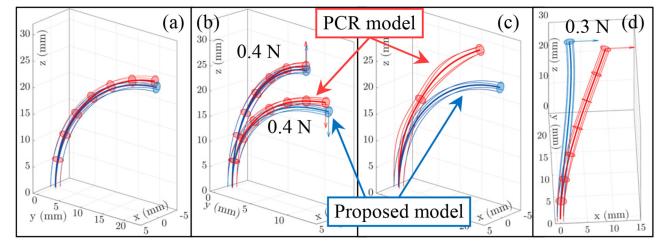


Fig. 8. Comparison between the proposed model (in blue) and the PCR model in [28] (in red): (a) no-load bending, (b) under planar external forces, (c) with sparse spacer rings, and (d) under an out-of-plane force.

Figure 7(b) presents the stiffness for both cases under external tip forces in the x, y and z directions. The continuum segment was shown to have higher stiffness than the Cosserat rod with lumped parameters with respect to different segment lengths and bending angles. This is because that disturbing the continuum segment from its bent configuration will lead to additional axial elongations/compressions of the backbone rods. It shall also be noted that the bending stiffness of the continuum segment is much lower than the stiffness of the four rods viewed as a continuum beam, since rods are only attached at the distal end and slide with respect to each other.

Examining the nonlinear discrepancy in the tip stiffness between the multi-backbone variable curvature model and the lumped-parameter rod model, the lumped parameters will become functions of the bending angles and the segment lengths. This essentially necessitates the development of the proposed multi-backbone variable curvature model.

To further illustrate how the adopted assumptions affect the model accuracy, the proposed variable curvature model is compared to the model in [28] (termed as PCR model here). Shapes of a 38-mm continuum segment were obtained using both models as in Fig. 8. While using the PCR model, the assumptions 1), 2), 3) and 5) in Section II.B are not applied.

The tip position discrepancy was 3.07% and 20.14% of the length for the no-load condition in Fig. 8(a) & (c). The shape

discrepancy is larger in Fig. 8(c) due to the reduced spacer disk use such that the assumption 2) of continuous constraint does not hold any more. The smaller discrepancy in Fig. 8(a) & (b) indicates that the assumptions 3) and 5) play less significant roles. When an out-of-plane external force is applied to cause torsion, the tip position discrepancy was 19.03% of the length (still big) as in Fig. 8(d), even though many spacer disks are used for the PCR model. This is because sole use of the spacer disks does not prevent torsion. Hence the assumption 1) of torsion-free bending does not hold.

Since the structure of the continuum robot in Section III.A has been designed to minimize torsion during bending, enable the continuous constraint, only allow small-curvature bending, and realize differential elongation of the backbone rods, the shape discrepancy between the proposed variable curvature model and the actual shape was hence acceptably small.

## V. CONCLUSION

This letter proposes a variable curvature model for multi-backbone continuum robots. Based on the Cosserat rod theory and the modeling assumptions, a compact formulation was derived, incorporating both Cosserat-rod-based mechanics and multi-backbone structural constraints. The model was adopted for a two-segment continuum robot to experimentally validate the model's performance in terms of accuracy and computational efficiency.

The experimental results demonstrated that the variable curvature model achieves tip positioning error reduction up to 68.83%, while compared with the constant curvature model. The model was also shown to have agreeable shape characterization for the continuum robot under a known external load and the computational time met the need from real-time control tasks.

Future work of this letter shall be focused on the generalization of the variable curvature model, for example, with variable backbone routing profile. What's more, the variable curvature model can also be employed in combination with various sensing schemes to realize force/contact estimation or feedback control.

## REFERENCES

- [1] J. Burgner-Kahrs, D. C. Rucker, and H. Choset, "Continuum robots for medical applications: A survey," *IEEE Trans. Robot.*, vol. 31, no. 6, pp. 1261–1280, Dec. 2015.
- [2] M. C. Yip, J. A. Sganga, and D. B. Camarillo, "Autonomous control of continuum robot manipulators for complex cardiac ablation tasks," *J. Med. Robot. Res.*, vol. 2, no. 1, 2016, Art. no. 1750002.
- [3] H. B. Gilbert, J. Neimat, and R. J. Webster III, "Concentric tube robots as steerable needles: Achieving follow-the-leader deployment," *IEEE Trans. Robot.*, vol. 31, no. 2, pp. 246–258, Apr. 2015.
- [4] A. Légnier *et al.*, "Endoluminal surgical triangulation 2.0: A new flexible surgical robot. Preliminary pre-clinical results with colonic submucosal dissection," *Int. J. Med. Robot. Comput. Assist. Surg.*, vol. 13, no. 3, Sep. 2017, Letter e1819.
- [5] K. Xu, J. Zhao, and M. Fu, "Development of the SJTU unfoldable robotic system (SURS) for single port laparoscopy," *IEEE/ASME Trans. Mechatronics*, vol. 20, no. 5, pp. 2133–2145, Oct. 2015.
- [6] K. Xu and N. Simaan, "Actuation compensation for flexible surgical Snake-like robots with redundant remote actuation," in *Proc. IEEE Int. Conf. Robot. Automat.*, Orlando, Florida, USA, 2006, pp. 4148–4154.
- [7] D. B. Camarillo, C. R. Carlson, and J. K. Salisbury, "Configuration tracking for continuum manipulators with coupled tendon drive," *IEEE Trans. Robot.*, vol. 25, no. 4, pp. 798–808, Aug. 2009.
- [8] R. J. Webster and B. A. Jones, "Design and kinematic modeling of constant curvature continuum robots: A review" *Int. J. Robot. Res.*, vol. 29, no. 13, pp. 1661–1683, 2010.
- [9] M. M. Dalvand, S. Nahavandi, and R. D. Howe, "An analytical loading model for n-Tendon continuum robots," *IEEE Trans. Robot.*, vol. 34, no. 5, pp. 1215–1225, Oct. 2018.
- [10] R. Roy, L. Wang, and N. Simaan, "Modeling and estimation of friction, extension, and coupling effects in multisegment continuum robots," *IEEE/ASME Trans. Mechatronics*, vol. 22, no. 2, pp. 909–920, Apr. 2017.
- [11] N. Simaan, "Snake-Like units using flexible backbones and actuation redundancy for enhanced miniaturization," in *Proc. IEEE Int. Conf. Robot. Automat.*, 2005, pp. 3012–3017.
- [12] J. Ding, R. E. Goldman, K. Xu, P. K. Allen, D. L. Fowler, and N. Simaan, "Design and coordination kinematics of an insertable robotic effectors platform for single-port access surgery," *IEEE/ASME Trans. Mechatronics*, vol. 18, no. 5, pp. 1612–1624, Oct. 2013.
- [13] N. Sarli, G. D. Giudice, S. De, M. S. Dietrich, S. D. Herrell, and N. Simaan, "TURBot: A system for Robot-assisted transurethral bladder tumor resection," *IEEE/ASME Trans. Mechatronics*, vol. 24, no. 4, pp. 1452–1463, May 2019.
- [14] N. Simaan *et al.*, "Design and integration of a telerobotic system for minimally invasive surgery of the throat," *Int. J. Robot. Res.*, vol. 28, no. 9, pp. 1134–1153, 2009.
- [15] J. Zhao, X. Zheng, M. Zheng, A. J. Shih, and K. Xu, "An endoscopic continuum testbed for finalizing system characteristics of a surgical robot for NOTES procedures," in *Proc. IEEE/ASME Int. Conf. Adv. Intell. Mechatronics*, 2013, pp. 63–70.
- [16] B. He, Z. Wang, Q. Li, H. Xie, and R. Shen, "An analytic method for the kinematics and dynamics of a multiple-backbone continuum robot," *Int. J. Adv. Robotic Syst.*, vol. 10, no. 1, pp. 1–13, Jan. 2013.
- [17] T. Qu, J. Chen, S. Shen, Z. Xiao, Z. Yue, and H. Y. K. Lau, "Motion control of a bio-inspired wire-driven multi-backbone continuum minimally invasive surgical manipulator," in *Proc. IEEE Int. Conf. Robot. Biomimetics*, 2016, pp. 1989–1995.
- [18] W. S. Rone and P. Ben-Tzvi, "Continuum robot dynamics utilizing the principle of virtual power," *IEEE Trans. Robot.*, vol. 30, no. 1, pp. 275–287, Feb. 2014.
- [19] T. Mahl, A. Hildebrandt, and O. Sawodny, "A variable curvature continuum kinematics for kinematic control of the bionic handling assistant," *IEEE Trans. Robot.*, vol. 30, no. 4, pp. 935–949, Aug. 2014.
- [20] R. J. Roesthuis and S. Misra, "Steering of multisegment continuum manipulators using rigid-link modeling and FBG-based shape sensing," *IEEE Trans. Robot.*, vol. 32, no. 2, pp. 372–382, Apr. 2016.
- [21] H. Yuan, L. Zhou, and W. Xu, "A comprehensive static model of Cable-driven multi-section continuum robots considering friction effect," *Mechanism Mach. Theory*, vol. 135, pp. 130–149, May 2019.
- [22] H. Yuan, P. W. Y. Chiu, and Z. Li, "Shape-reconstruction-based force sensing method for continuum surgical robots with large deformation," *IEEE Robot. Automat. Lett.*, vol. 2, no. 4, pp. 1972–1979, Oct. 2017.
- [23] V. K. Venkiteswaran, J. Sikorski, and S. Misra, "Shape and contact force estimation of continuum manipulators using pseudo rigid body models," *Mechanism Mach. Theory*, vol. 139, No.no. 2019, pp. 34–45, Sep. 2019.
- [24] D. C. Rucker, I. Webster, J. Robert, G. S. Chirikjian, and N. J. Cowan, "Equilibrium conformations of concentric-tube continuum robots," *Int. J. Robot. Res.*, vol. 29, no. 10, pp. 1263–1280, Sep. 2010.
- [25] D. C. Rucker and R. J. Webster, "Statics and dynamics of continuum robots with general tendon routing and external loading," *IEEE Trans. Robot.*, vol. 27, no. 6, pp. 1033–1044, Dec. 2011.
- [26] D. C. Rucker, B. A. Jones, and R. J. Webster, "A geometrically exact model for externally loaded concentric-tube continuum robots," *IEEE Trans. Robot.*, vol. 26, no. 5, pp. 769–780, Oct. 2010.
- [27] C. E. Bryson and D. C. Rucker, "Toward parallel continuum manipulators," in *Proc. IEEE Int. Conf. Robot. Automat.*, 2014, pp. 778–785.
- [28] A. L. Orekhov, V. A. Aloï, and D. C. Rucker, "Modeling parallel continuum robots with general intermediate constraints," in *Proc. IEEE Int. Conf. Robot. Automat.*, 2017, pp. 6142–6149.
- [29] K. Xu and N. Simaan, "An investigation of the intrinsic force sensing capabilities of continuum robots," *IEEE Trans. Robot.*, vol. 24, no. 3, pp. 576–587, Jun. 2008.
- [30] S. A. Zhang, Q. Li, H. Yang, J. Zhao, and K. Xu, "Configuration transition control of a continuum surgical manipulator for improved kinematic performance," *IEEE Robot. Automat. Lett.*, vol. 4, no. 4, pp. 3750–3757, Oct. 2019.
- [31] K. Xu *et al.*, "Preliminary development of a continuum dual-arm surgical robotic system for transurethral procedures," in *Proc. Int. Conf. Intell. Robot. Appl.*, 2017, pp. 311–322.
- [32] A. Bajo and N. Simaan, "Hybrid motion/force control of multi-backbone continuum robots," *Int. J. Robot. Res.*, vol. 35, no. 4, pp. 422–434, 2015.